Supplemental Material for "*The sites of evaporation within leaves*" by Thomas N. Buckley, Grace P. John, Christine Scoffoni and Lawren Sack

Boundary conditions, solution and vapor phase transport in the MOFLO 2.0 model

(Ia) Matrix/vector expression of mass and energy balance and calculation of boundary exchanges

The systems of linear equations described by Equations 1-7 in Methods of the main text can be expressed in matrix/vector form. However, the equations for nodes at the leaf surfaces must be modified to account for exchanges across the boundary between the system (the outside-xylem compartment of a leaf areole) and the surrounding atmosphere. The matrix/vector forms of the conservation equations are:

(S1) $0 = \mathbf{L} + \mathbf{V}$,

(S2) $0 = \mathbf{Q} + \mathbf{H} + \lambda\mathbf{V}$, and

(S3) $\mathbf{V} = \mathbf{G} + \mathbf{F} + \mathbf{E}$,

where **L** and **V** are net rates of water loss in the liquid and vapor phase, respectively; **Q** is net loss of energy by radiation exchange with the environment surrounding the leaf, **H** describes net sensible heat loss and the product λ**V** represents the net latent heat loss (evaporative cooling), where λ is the latent heat of vaporization; **V** is the sum of net isothermal (**G**) and anisothermal (**F**) losses, as well as losses to the surrounding atmosphere (**E**). Most these vectors can be expressed as products of matrices of conductances for either heat or mass transport, and vectors of the state variables (temperature **T** and water potential ψ) whose gradients drive heat and mass transport. For example, net liquid-phase mass loss can be written as the product of a matrix $\mathbf{K}_l$ of liquid-phase hydraulic conductances and a vector ψ whose elements are the water potentials at each node:

(S4) $\mathbf{L} = \mathbf{K}_l\psi$.

Similarly, for isothermal and anisothermal vapor transport (IVT and AVT, respectively),

(S5) $\mathbf{G} = \mathbf{K}_g\psi$,

(S6) $\mathbf{F} = \mathbf{K}_f\mathbf{T}$,

where $\mathbf{K_g}$ and $\mathbf{K_f}$ are matrices of isothermal and anisothermal vapor phase conductances for mass transport, respectively (cf. Eqn S26 below). Sensible heat loss can also be represented in the same fashion:

(S7) $$\mathbf{H} = \mathbf{K_h}\mathbf{T}.$$

Exchanges across the system boundary require modification of some terms in these vectors. For example, the equations describing isothermal vapor mass balance for epidermal nodes include a term that depends on the water vapor mole fraction of the ambient air, w_{air}:

(S8) $$G'_i = \sum_j K_{g,ij}\left(\psi_i - \psi_j\right) + g_{tw}a_i\left(w_i - w_{air}\right),$$

where g_{tw} is the leaf-to-air conductance to water vapor (including stomatal and boundary layer components; mol m^{-2} s^{-1}), a_i is the leaf surface area of node i (m^2), and w_{air} is ambient water vapor mole fraction (mol mol^{-1}). Applying $w_i \approx w'_s \cdot (\psi_i \cdot v_w/RT + 1)$ (from Eqn 11 in Buckley, 2015), where w'_s is the saturated water vapor mole fraction evaluated at the leaf surface temperature T, to Eqn S8 and rearranging terms leads to

(S9) $$G'_i = \left(\sum_j K_{g,ij} + K_{g,ia}\right)\psi_i - \sum_j K_{g,ij}\psi_j + g_{tw}a_i\left(w'_s - w_{air}\right),$$

where $K_{g,ia} = g_{tw} \cdot a_i \cdot w'_s \cdot v_w/RT$. The term involving g_{tw} in Eqn S9 cannot be included in the vector **G** if **G** is to be written as a product of a matrix of conductances ($\mathbf{K_g}$) and the vector of water potentials within the leaf grid ($\boldsymbol{\psi}$). Therefore, the term G'_i in Eqns S8 and S9 is written with a prime symbol to distinguish it from the value of G_i that corresponds to Eqn S5 as we actually implemented it: we include the term involving g_{tw} in Eqn S9 in another vector, **E**, whose elements E_i represent the components of net mass losses across the system boundary that are independent of the water potential of nodes at the system boundary, thus:

(S10) $$E_i = g_{tw}a_i\left(w'_s - w_{air}\right),$$

and we define $G_i \equiv G'_i - E_i$ for epidermal nodes. E_i is very close to, but not in general exactly equal to the actual transpiration rate for node i, because in general w_i will not be exactly equal to w'_s; a very

small part of the transpiration rate is directly affected by the water potential of node *i*, and that part of the transpiration rate is captured by G_i (specifically, by the first term on the right-hand side of Eqn S9, involving $K_{g,ia}$). A similar issue arises with convective heat exchange at surface nodes, which include a term that depends on ambient air temperature, T_{air}:

(S11) $$H_i' = \sum_i K_{h,ij}\left(T_i - T_j\right) + K_{h,ia}\left(T_i - T_{air}\right) = \left(\sum_i K_{h,ij} + K_{h,ia}\right)T_i - \sum_i K_{h,ij}T_j - K_{h,ia}T_{air}\,.$$

where $K_{h,ia} = g_{bh}\cdot c_{pair}\cdot a_i$, where g_{bh} is the boundary layer conductance of a single leaf surface to heat transfer and c_{pair} is the heat capacity of the air (29.3 J mol^{-1} K^{-1}). In this case, the term $K_{h,ia}\cdot T_{air}$ cannot be included in **H** if **H** is to be defined as $\mathbf{K_hT}$ (Eqn S7a), so we incorporated this term into a vector **Q** describing net energy losses across the system boundary. **Q** also includes net losses by longwave radiation (which we assumed occur only from surface nodes and are functions of surface temperature) and shortwave radiation, I_i (the latter being negative if expressed as loss terms, because the leaf absorbs rather than emits shortwave radiation). Thus, we write Q_i as

(S12) $$Q_i = \varepsilon_{leaf}\sigma\left(T_i^4 - T_{sky}^4\right) - I_i - K_{h,ia}T_{air}\,,$$

where T_{sky} is the effective radiative temperature of the external environment seen by the leaf, ε_{leaf} is leaf emissivity to IR, and σ is the Stefan-Boltzmann constant. Note that $K_{h,ia}$ is only nonzero for epidermal nodes, because other nodes do not contact the air directly. We calculated T_{sky} from ambient air temperature as $T_{sky} = \varepsilon_{atm}^{0.25}\cdot T_{air,K}$, where $T_{air,K}$ is T_{air} in kelvins and atmsopheric emissivity $e_{atm} = 0.84\cdot f_{cloud} + (1 - 0.84\cdot f_{cloud})\cdot 1.72\cdot(e_{air}/T_{air,K})^{1/7}$ (Campbell and Norman, 1998), where f_{cloud} is the fraction of the sky covered by cloud (assumed 0.5 here) and ambient humidity $e_{air} = w_a\cdot p_{total}/1000$ (with p_{total} in Pa, this gives e_{air} in kPa). We modeled absorbed shortwave radiation, I_i, as

(S13) $I_i = I_{VIS,i} + I_{NIR,i}$, where

(S14) $$I_{VIS,i} = \tfrac{1}{2}0.566\cdot p\begin{pmatrix} I_u\left(\exp\left(-k_c C_{i,top}\right) - \exp\left(-k_c C_{i,bottom}\right)\right) \\ +\tau I_l\left(\exp\left(k_c C_{i,bottom}\right) - \exp\left(k_c C_{i,top}\right)\right)\end{pmatrix}, \text{ and}$$

(S15) $$I_{NIR,i} = \tfrac{1}{2}0.566\cdot 0.10\cdot\left(1-\tau\right)\left(I_u + I_l\right)\left(t_i/t_{total}\right),$$

where $I_{VIS,i}$ and $I_{NIR,i}$ are the visible and near-infrared (NIR) radiation absorbed by layer i, respectively; I_u and I_l are photosynthetic photon flux density (PPFD) incident on the upper and lower surfaces,

respectively (I_l is included for the sake of completeness, but was set at zero in all simulations shown here); $\tau = \exp(-k_c \cdot C_{total})$ is leaf transmittance to non-reflected light, where C_{total} is total leaf chlorophyll content and k_c is the sum of absorption and scattering coefficients for PPFD within the leaf; $C_{i,top}$ and $C_{i,bottom}$ are the cumulative chlorophyll contents at the top and bottom of node *i*, respectively (measured relative to the upper surface where $C_{i,top} = 0$); t_i and t_{total} are the thickness of layer i and the entire leaf, respectively; and p accounts for surface reflectance and scattering within the leaf (for simplicity we assumed $p \approx 1$, which is consistent with ray-tracing simulations of light propagation within leaves (Ustin et al., 2001)). The factor 0.566 (J μmol^{-1} photons) is the ratio of total shortwave energy (visible and NIR combined) to photosynthetic photon flux in extraterrestrial solar radiation (de Pury and Farquhar, 1997); about half of this energy is visible and half NIR, which gives rise to the 1/2 factors in Eqns S14 and S15. Equation S14 is based on a model of paradermal light propagation given by Buckley and Farquhar (2004); specifically, it is the integral of their Eqn 2 between the top and bottom of node i. Equation S15 assumes that NIR absorption is equally distributed among leaf layers due to high the scattering coefficient for NIR (e.g., Gates et al., 1965). The factor 0.10 in Eqn S15 assumes that the overall leaf absorptance to NIR is 10% that for visible light; the actual ratio varies across species from about 5 to 20% (Gates et al., 1965; Feret et al., 2008), but we found its exact value had little impact on our simulations.

We calculated the Chl content of each node, and hence $C_{i,top}$ and $C_{i,bottom}$ for each node, from the chlorophyll density per unit tissue volume in the palisade and spongy mesophyll, which we in turn estimated from measurements of leaf chlorophyll concentration and tissue dimensions (John et al., 2013) in each of 12 of our 14 species. We measured chlorophyll content before noon in three leaves from three individuals per species using a SPAD-502 instrument (Spectrum Technologies, IL, USA), averaging readings at the proximal, middle and distal leaf regions (avoiding the midrib and leaf margin) and converting SPAD to Chl content using the average from two cross-species calibration curves (Markwell et al., 1995; Coste et al., 2010). Total chlorophyll content (C_{total}, mmol m^{-2}) was calculated as $\rho_{c,pal} \cdot t_{pal} + \rho_{c,spo} \cdot t_{spo} + \rho_{c,epid} \cdot (t_{eu} + t_{el})$, where $\rho_{c,pal}$, $\rho_{c,spo}$ and $\rho_{c,epid}$ are the chlorophyll densities (mmol Chl m^{-3}) for palisade, spongy and epidermis, respectively, and t_{pal}, t_{spo}, t_{eu} and t_{el} are tissue thicknesses (μm) for palisade, spongy and upper and lower epidermis, respectively. True chlorophyll density for epidermis may be negligible, but we treated it as nonzero to account for absorption of visible light by substances other than chlorophyll; comparison of albino and normal leaves suggests achlorophyllous tissues absorb approximately 5% as much visible light as chlorophyllous tissues (Jacquemoud and Baret, 1990), so we assumed $\rho_{c,epid} = 0.05 \cdot \rho_{c,pal}$. We further assumed that the chlorophyll density per unit cell volume was identical in the palisade and spongy

mesophyll, so that $\rho_{c,pal}$ and $\rho_{c,spo}$ differed only due to differences in airspace fraction; thus, $\rho_{c,spo} = \rho_{c,pal}\cdot(1 - p_S)/(1 - p_P)$, where p_S and p_P are spongy and palisade airspace fractions, respectively. Thus, $\rho_{c,pal} = C_{total}/(0.05\cdot(t_{eu}+t_{el}) + t_p + t_s\cdot(1-p_s)/(1-p_p))$. Finally $C_{i,bottom} - C_{i,top} = \rho_{ci}\cdot t_i$, where ρ_{ci} is the Chl density appropriate to a given layer, and $C_{i,top} = 0$ by definition for nodes at the upper leaf surface. For BS and BSE nodes, we assumed the same effective Chl density as epidermal nodes. We estimated the value of k_c (the chlorophyll-specific extinction coefficient in Eqn S14) by adjusting it for each species so that the species' PPFD absorptance calculated from its measured total Chl content based on Eqn S14 (i.e., $1 - \exp(-k_c\cdot C_{total})$) equalled the value calculated using Evans's (1998) expression relating PPFD absorptance to C_{total} across several species (i.e., $C_{total}/(C_{total} + 0.076)$), and then taking the average of the resulting fitted k_c values across species (k_c = 3.69 m^2 $mmol^{-1}$Chl). We lacked C_{total} measurements for *H. annuus* and *R. coulteri*; for *H. annuus*, we used the average of two values reported by Jacob and Lawlor (1991) (0.58 mmol m^{-2}), and for *R. coulteri*, we estimated C_{total} by multiplying the mean whole-leaf Chl density from the other 12 species (2.34 mmol m^{-3}) by mean leaf thickness for *R. coulteri* (369 μm) to give 0.86 mmol m^{-2}.

(Ib) Solving the system

The system outlined above represents a set of coupled matrix equations in $\boldsymbol{\psi}$ and **T** as dependent variables. The solution is outlined below. First, applying Eqns S5, S6 and S7 to Eqn S2 and solving for $\boldsymbol{\psi}$ gives

(S16) $\boldsymbol{\psi} = -\mathbf{K}_1'\mathbf{T} - \boldsymbol{\psi}_1'$, where

(S16a) $\mathbf{K}_1' \equiv \mathbf{K}_\mathbf{g}^{-1}\left(\lambda^{-1}\mathbf{K}_\mathbf{h} + \mathbf{K}_\mathbf{f}\right)$ and

(S16b) $\boldsymbol{\psi}_1' \equiv \mathbf{K}_\mathbf{g}^{-1}\left(\lambda^{-1}\mathbf{Q} + \mathbf{E}\right)$

Second, applying Eqns S4, S5, S6 to Eqn S1 and solving for $\boldsymbol{\psi}$ gives

(S17) $\boldsymbol{\psi} = -\mathbf{K}_2'\mathbf{T} - \boldsymbol{\psi}_2'$, where

(S17a) $\mathbf{K}_2' \equiv \left(\mathbf{K}_\mathbf{l} + \mathbf{K}_\mathbf{g}\right)^{-1}\mathbf{K}_\mathbf{f}$ and

(S17b) $\boldsymbol{\psi}_2' \equiv \left(\mathbf{K}_\mathbf{l} + \mathbf{K}_\mathbf{g}\right)^{-1}\mathbf{E}$

Third, setting the two $\boldsymbol{\psi}$ solutions equal to one another leads to a solution for **T**:

(S18) $$\mathbf{T} = \left[\mathbf{K}'_2 - \mathbf{K}'_1\right]^{-1}\left[\boldsymbol{\psi}'_1 - \boldsymbol{\psi}'_2\right].$$

Finally, applying this solution for **T** to either Eqn S16 or S17 leads to a solution for $\boldsymbol{\psi}$.

Because the boundary exchanges and anisothermal vapor conductances depend on leaf temperature, yet leaf *T* is also predicted by the system, we solved the system iteratively, by imposing an initial guess for surface temperatures, updating them based on the results from Eqn S18, and repeating this process. For the first three iterations, we reduced the spatial resolution of the grid to 10 x 10 nodes, and then increased it to the final size (either 20 x 20 or 30 x 30 depending on the simulation) before repeating one more iteration. We found that changes in computed system properties were generally negligible after the first pair of iterations, and that surface temperatures also changed negligibly after switching to the higher-resolution grid.

(Ic) Isothermal and anisothermal vapor transport

Buckley (2015) showed that vapor phase transport could be separated into two components: one driven by water potential gradients and approximately independent of temperature gradients (the "isothermal" component), and another driven by temperature differences and approximately independent of water potential (the "anisothermal" component). The intrinsic hydraulic conductivity for isothermal vapor transport (Eqn 15 in Buckley et al, 2015) is

(S19) $$k_{g,iso} = \frac{D_{wa} V_w p_{sat}}{\left(R_{gas} T\right)^2},$$

where D_{wa} is the molecular diffusivity of water vapor in air and p_{sat} is the saturation vapor pressure at temperature *T*. Although $k_{g,iso}$ does depend on temperature, it varies only negligibly under the temperature gradients simulated within leaves, which are on the order of 0.1 K. The intrinsic hydraulic conductivity for anisothermal vapor transport from node *i* to node *j* is

(S20) $$k_{g,aniso,ij} = \frac{D_{wa}}{\left(\psi_i - \psi_j\right) R_{gas}} \left(\frac{p_{sat,i}}{T_i} - \frac{p_{sat,j}}{T_j} \right) \left(1 + \frac{\psi_i V_w}{R_{gas} T_j} \right),$$

where $p_{sat,i}$ and $p_{sat,j}$ are the saturation vapor pressures at T_i and T_j, respectively. For ψ_i in typical operating ranges, the ψ-dependent term in parentheses at right is negligible (this is Eqn 16 in Buckley et al. 2015). Note also that the corresponding vapor flux is obtained by multiplying $k_{g,aniso,ij}$ by

the water potential gradient from node *i* to node *j*, $\psi_i - \psi_j$. Thus, the anisothermal vapor flux from node *i* to node *j*, F_{ij}, is approximately

$$F_{ij} = \frac{D_{wa}}{R_{gas}}\left(\frac{p_{sat,i}}{T_i} - \frac{p_{sat,j}}{T_j}\right). \quad \text{(S21)}$$

This can be rearranged as

$$F_{ij} = \frac{D_{wa}}{R_{gas}T_iT_j}\left(p_{sat,i}T_j - p_{sat,j}T_i\right). \quad \text{(S22)}$$

Across small temperature ranges, $p_{sat,i}$ is approximately a linear function of temperature:

$$p_{sat} \approx sT - b\,, \quad \text{(S23)}$$

where *s* and *b* are positive constants that depend on the temperature range and can be estimated from the relationship between p_{sat} and *T*. Applying Eqn S23 to Eqn S22 gives

$$F_{ij} = \frac{D_{wa}}{R_{gas}T_iT_j}\left(\left(sT_i - b\right)T_j - \left(sT_j - b\right)T_i\right), \quad \text{(S24)}$$

and rearranging leads to

$$F_{ij} = \frac{D_{wa}b}{R_{gas}T_iT_j}\left(T_i - T_j\right). \quad \text{(S25)}$$

For the small temperature gradients that occur within a single leaf areole, variation in the product $T_i \cdot T_j$ is negligible, so it can be replaced by the square of an estimate of the prevailing leaf temperature, *T*, with minimal error:

$$F_{ij} = \frac{D_{wa}b}{R_{gas}T^2}\left(T_i - T_j\right). \quad \text{(S26)}$$

Thus, anisothermal vapor flux can be modeled as a product of a "heat-coupled mass conductance", $k_{g,aniso} = D_{wa}b/(R_{gas}T^2)$, and a temperature difference, as shown in Eqn S6. Note as well that

(S27) $$k_{g,aniso} = \frac{D_{wa}b}{R_{gas}T^2} = \left(\frac{bR_{gas}}{V_w p_{sat}}\right)k_{g,iso}.$$

Given $p_{sat}(T) = 611.2\cdot\exp(17.62\cdot(T - 273.15)/(T - 30.03))$ for T in kelvins, and assuming $p_{sat} \approx mT - b$ (Eqn S23), it follows that $b \approx T\cdot dp_{sat}/dT - p_{sat}(T) = p_{sat}(T)\cdot(\mathrm{dln}p_{sat}/\mathrm{dln}T - 1)$ for some T in a narrow range of interest. $\mathrm{dln}p_{sat}/\mathrm{dln}T$ is easily computed as $4283.8\cdot T/(T - 30.03)^2$, which gives b as

(S28) $$b \approx p_{sat}(T)\left(\frac{4283.8\cdot T}{(T - 30.03)^2} - 1\right).$$

The approximations upon which Eqns S19 and S26 are based introduce less than 3% error across a wide range of temperature gradients, ambient temperatures and water potentials (as low as -4 MPa, lower than we simulated for any point within the leaves of any species in this study), and these errors were on the order of 0.5 – 1% under conditions typical of mean simulation output; this is shown in Fig S4.

(1d) Modeling the bundle sheath apoplast separately

MOFLO 2.0 assumes that apoplastic, transmembrane/transcellular and vapor phase pathways operate in parallel among nodes in the grid. That assumption is suitable for assessing transport among tissue types, but it is unsuitable for accurately attributing evaporation to individual nodes in the rare case where the transport pathways only operate in series within a particular tissue. The only instance where this occurs in MOFLO 2.0 is for water transport from the bundle sheath to adjacent tissues: in the case where BS apoplastic transport is suppressed by assumption in the model (to represent an hypothesised apoplastic barrier due to suberization and/or lignification of anticlinal BS cell walls), water is forced to move from the interior of the BS to adjacent nodes first via the transmembrane pathway, and then via any available transport modes between the BS and adjacent tissues. Only the water potential drawdown from the apoplast to distal nodes – and not the drawdown across the membrane – is relevant to computing vapor transport. Therefore, in order to accurately compute the vapor phase flow between the BS and the mesophyll in this situation, it is necessary to break the water potential drawdown from BS nodes to the mesophyll into two steps (across the BS membrane, and then from the BS apoplast to the mesophyll), and only use the latter

part of the gradient to compute vapor phase flow. This requires defining an additional node between the BS and the mesophyll, which represents the outer BS apoplast (i.e., the surface facing towards the mesophyll). Therefore, for the present study, we defined the nodes immediately distal to the BS (i.e., in the rows above and below, and in the column to the right) as BS apoplast nodes. Bulk conductivities for connections between adjacent tissues are computed as the inverse of the sums of one-half of each tissue's conductivity in the direction in question (e.g., for a horizontal BS-spongy mesophyll connection, the conductivity would be $1/(0.5/k_{BS,horz} + 0.5/k_{SPO,horz})$, where $k_{BS,horz}$ and $k_{SPO,horz}$ are the bulk conductivities for horizontal water transport through the BS and spongy mesophyll, respectively, as defined by Buckley et al. (2015)). For the present study, we separated these conductivities to simulate flow into or out of the intervening BS apoplast node (e.g., the BS to BS-apoplast conductivity would be $2 \cdot k_{BS,horz}$ and the BS-apoplast to spongy conductivity would be $2 \cdot k_{SPO,horz}$).

Measurements of internal and cellular dimensions of leaves at turgor loss point

To quantify changes in tissue and cellular dimensions during dehydration, we used x-ray micro-computed tomography (microCT) at the synchrotron at the Advanced Light Source (ALS) in Berkeley, California (Beamline 8.3.2) in November of 2014 (Scoffoni et al., in press). Stacks of images were obtained by scanning the center of leaves still attached to shoots that had been dehydrated to the species' turgor loss point. Leaf scans were performed for three of our study species (*Comarostaphylis diversifolia, Hedera canariensis*, and *Lantana camara*). Three to four scans of the midrib and surrounding mesophyll at the center of leaf were made per species at around their turgor loss point. We randomly selected three cross-sectional images at the bottom, middle and top part along the main axis of the microCT 3D rendering scans obtained. For each image mesophyll cell and tissue dimensions were quantified using ImageJ software (version 1.46r; National Institutes of Health). For each image we measured and averaged at three areas of the leaf lamina the tissue height and cell area and diameter of the epidermis, cuticle, palisade and spongy mesophyll. Because bundle sheath cell dimensions could not be resolved in these images, we assumed they shrunk in equal proportion to that of the spongy mesophyll. The percent leaf area shrinkage at turgor loss point and percent intercellular airspace change was obtained from previously published data for these same species and individuals by gradually dehydrating leaves on the bench and repeatedly measuring leaf thickness, area and mass (Scoffoni et al., 2014). To obtained the percent change in intercellular airspace, we assumed the change in total leaf thickness was due to loss of water and change in intercellular airspace, with dry mass staying constant as the leaf dehydrated.

Table S1. Percent changes in anatomical parameters between full turgor and turgor loss point in three species.

	species		
parameter	*C. diversifolia*	*H. canariensis*	*L. camara*
palisade tissue thickness	-35.0	-64.4	-68.2
spongy tissue thickness	-15.0	-49.9	-69.4
upper epidermis thickness	-23.0	-43.0	-29.6
lower epidermis thickness	-48.2	-37.6	-48.8
palisade cell height	-17.4	-47.8	-64.7
palisade cell radius	-38.7	-50.3	-55.5
spongy cell radius	-31.3	-44.2	-62.8
airspace fraction	+12.4	+114.9	-67.2
VLA	+0.9	+1.6	+9.9

Table S2. Anatomical parameter values for the 14 species used in this study.Anatomical parameter values measured for 14 species. Species codes are: BAGA, *Bauhinia galpinii*; CASA, *Camellia sasanqua*; CEBE, *Cercocarpus betuloides*; CODI, *Comarostophylos diversifolia*; HEAN, *Helianthus annuus*; HEAR, *Heteromeles arbutifolia*; HECA, *Hedera canariensis*; LACA, *Lantana camara*; MAGR, *Magnolia grandiflora*; PLRA, *Platanus racemosa*; QUAG, *Quercus agrifolia*; RAIN, *Raphiolepis indica*; ROCO, *Romneya coulterii*, SACA, *Salvia canariensis*.

			species												
parameter	**symbol**	**units**	**BAGA**	**CASA**	**CEBE**	**CODI**	**HEAN**	**HEAR**	**HECA**	**LACA**	**MAGR**	**PLRA**	**QUAG**	**RAIN**	**ROCO**	**SACA**
cell wall thicknesses																
bundle sheath cell wall thickness	t_{abs}	µm	0.56	0.99	0.69	0.73	0.63	1.71	1.21	0.83	1.14	0.79	1.02	1.14	0.82	0.75
epidermal cell wall thickness (lower)	t_{ael}	µm	0.63	2.54	1.74	2.03	0.80	1.80	1.84	1.55	2.40	1.48	1.80	2.10	1.96	1.22
epidermal cell wall thickness (upper)	t_{aeu}	µm	0.95	2.93	2.24	2.67	0.80	1.76	1.98	1.56	2.30	1.66	1.97	1.94	2.04	1.42
palisade cell wall thickness	t_{ap}	µm	0.54	1.48	1.08	1.41	0.66	1.18	1.48	1.06	1.73	0.81	1.23	1.17	1.36	0.93
spongy cell wall thickness	t_{as}	µm	0.64	2.15	1.30	1.23	0.54	1.37	1.77	1.09	1.76	0.81	1.53	1.92		0.91
BSE cell wall thickness	t_{ax}	µm	1.07		1.42	1.26	1.54				2.30	0.69	1.34		1.34	
cell scale parameters																
palisade cell height	h_p	µm	27.9	69.4	29.3	47.4	48.1	43.6	45.3	39.8	60.8	50.9	35.0	47.0	36.6	34.2
bundle sheath cell perimeter	p_{bsc}	µm	28.3	69.6	40.1	46.7	55.5	69.7	80.5	59.8	66.4	47.6	47.0	73.2	58.3	37.6
palisade radius	r_p	µm	6.7	20.9	8.0	14.1	14.4	10.5	26.8	11.7	21.6	11.7	8.7	11.5	12.6	12.4
spongy radius	r_s	µm	9.0	27.8	6.0	19.7	17.2	22.0	25.0	14.6	24.6	11.1	10.4	25.5		11.3
width of upper epidermal cell	w_{el}	µm	11.2	25.0	9.4	11.1	19.2	17.6	21.7	14.0	19.9	18.4	11.1	14.1	41.7	13.6
width of lower epidermal cell	w_{eu}	µm	16.4	12.5	18.1	15.6	14.9	21.5	10.5	16.4	18.0	18.4	18.7	39.6	42.0	16.2
width of one BSE cell	w_x	µm	8.2		19.9	18.6	34.3				23.1	9.4	16.3		28.5	
tissue scale parameters																
distance from BS to lower epid	h_{xltot}	µm	7.7	111.5	47.9	73.9	52.7	97.7	121.5	30.3	145.0	39.2	41.0	195.1	76.0	41.7
distance from BS to upper epid	h_{xutot}	µm	29.8	94.3	113.8	140.9	70.9	92.9	112.1	77.3	220.2	76.2	140.3	126.8	92.3	65.4
total perimeter of vascular bundle	p_{bs}	µm	143.9	391.3	247.1	300.5	195.7	525.2	288.0	273.0	343.6	194.7	282.3	399.1	359.5	185.2
lower epidermis thickness	t_{el}	µm	9.5	13.1	18.9	8.5	11.3	17.6	9.2	10.4	10.1	11.1	12.5	13.9	34.1	8.9
upper epidermis thickness	t_{eu}	µm	16.0	13.9	19.0	14.8	13.3	18.9	11.0	18.4	47.4	17.9	19.1	36.8	40.4	16.2
palisade thickness	t_p	µm	27.6	121.9	97.6	100.8	67.2	95.1	66.1	85.7	195.4	72.4	118.9	107.2	294.3	87.0
spongy thickness	t_s	µm	37.5	259.0	112.5	160.6	90.6	236.4	215.5	93.3	268.2	93.5	127.5	304.5		66.2
total width of BSE	w_{xtot}	µm	15.3		21.1	31.2	13.2				40.4	6.2	26.4		17.7	
dimensionless parameters																
palisade horizontal connectivity	f_{cph}	-	0.42	0.22	0.18	0.22	0.22	0.07	0.03	0.21	0.52	0.49	0.74	0.85	0.57	0.60
palisade vertical connectivity	f_{cpv}	-	0.44	0.49	0.35	0.58	0.42	0.64	0.64	0.62	0.43	0.28	0.36	0.24	0.24	0.33
spongy mesophyll connectivity	f_{cs}	-	0.31	0.50	0.17	0.21	0.23	0.32	0.28	0.17	0.23	0.28	0.23	0.24		0.23
leaf airspace fraction in palisade	p_p	-	0.10	0.20	0.12	0.10	0.27	0.23	0.13	0.18	0.18	0.40	0.07	0.12	0.35	0.20
leaf airspace fraction in spongy	p_s	-	0.10	0.42	0.63	0.40	0.43	0.60	0.52	0.33	0.32	0.45	0.27	0.40		0.27
leaf scale parameters																
vein length per unit area	VLA	mm^{-1}	4.98	3.31	7.74	4.17	9.32	4.63	3.00	9.75	5.16	4.97	7.30	3.90	4.15	4.15

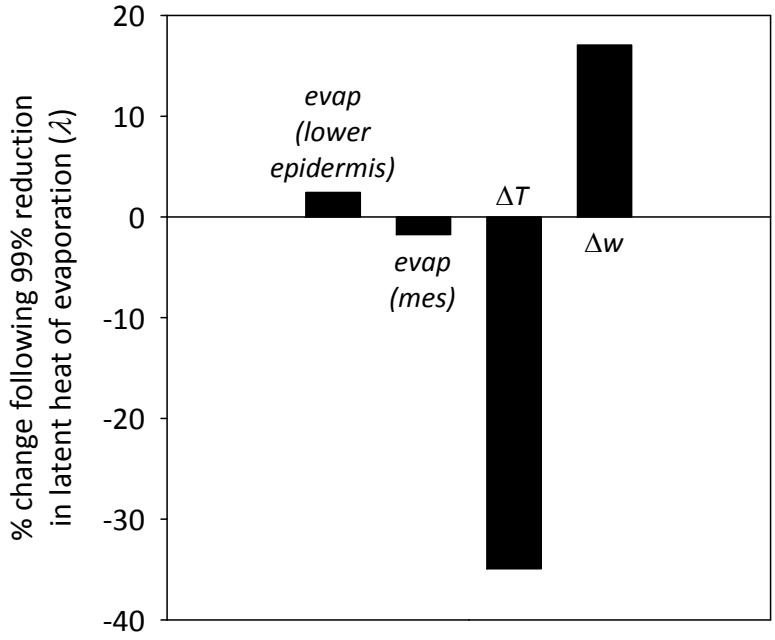

Figure S1. Evaporative cooling within the leaf is not an important determinant of where evaporation occurs: a simulated 99% reduction in evaporative cooling (achieved by reducing the latent heat of evaporation, λ, by 99%) caused only very small changes in the partitioning of evaporation between the lower epidermis (EL) and mesophyll (mes), despite large effects on the vertical temperature gradient within leaves (ΔT) and the leaf to air water vapor mole fraction gradient (Δw).

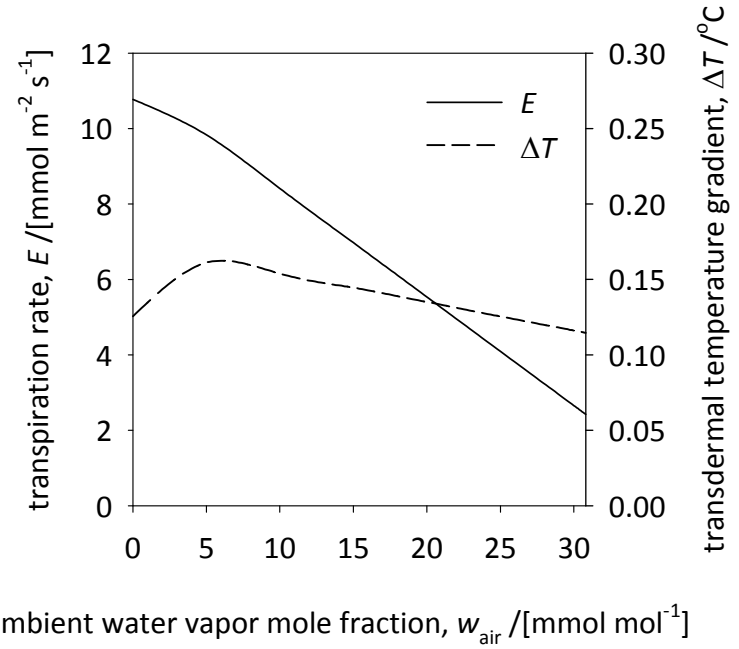

Figure S2. Changes in transpiration rate and vertical intra-leaf temperature gradient in relation to changes in ambient water vapor mole fraction of the air (means across 14 species listed in Table III of the main text). Photosynthetic photon flux density was 1500 μmol m^{-2} s^{-1} and air temperature was 25 °C.

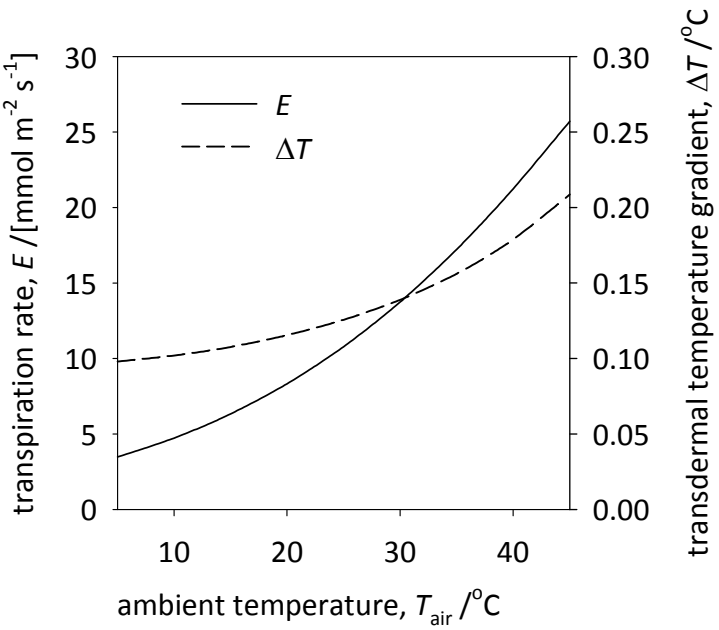

Figure S3. Changes in transpiration rate and vertical intra-leaf temperature gradient in relation to changes in ambient air temperature (means across 14 species listed in Table III of the main text). Photosynthetic photon flux density was 1500 μmol m^{-2} s^{-1} and ambient water vapor mole fraction was zero (note, the default value for ambient humidity was 15 mmol mol^{-1} in most other simulations, but was set at zero in simulations for this figure to prevent ambient relative humidity from exceeding 100%).

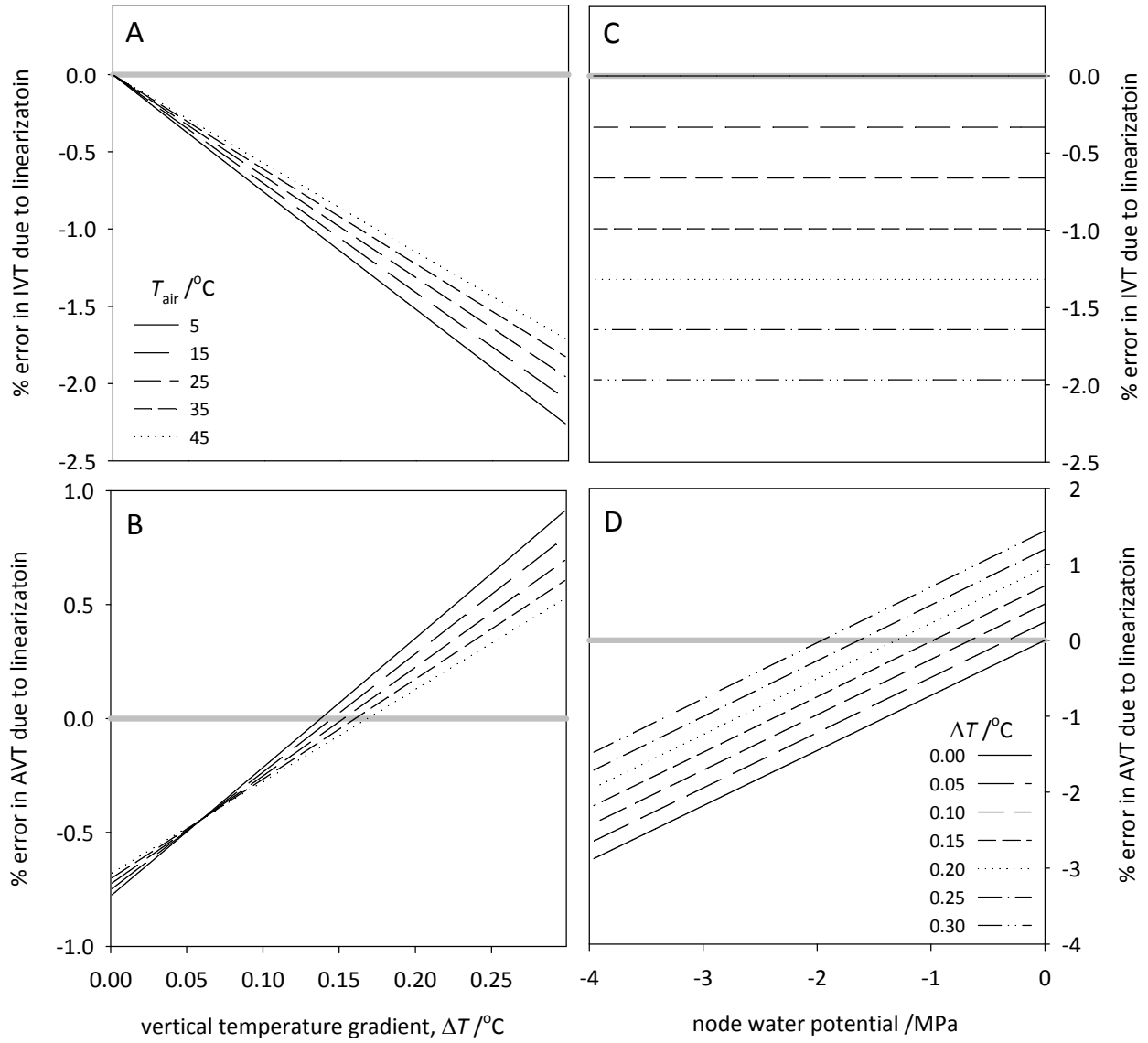

Figure S4. Percent error introduced into the node-to-node conductance, $k_{g,iso}$, for isothermal vapor transport (IVT; panels A and C), and the node-to-node anisothermal vapor flux (AVT; panels B and D) as a result of the approximations presented in the main text, assuming (A,B) a vertical temperature gradient within the leaf as shown, equally distributed across nodes, giving a node-to-node T gradient 1/30th of the values shown in the x-axis, or (C,D) a nodal water potential as shown. Calculations are shown for a range of values for air temperature in A and B, or for nodal water potential in C and D. For reference, the mean simulated temperature gradient and nodal water potential across species at 25 °C were 0.145 °C and -1.44 MPa, respectively.

351

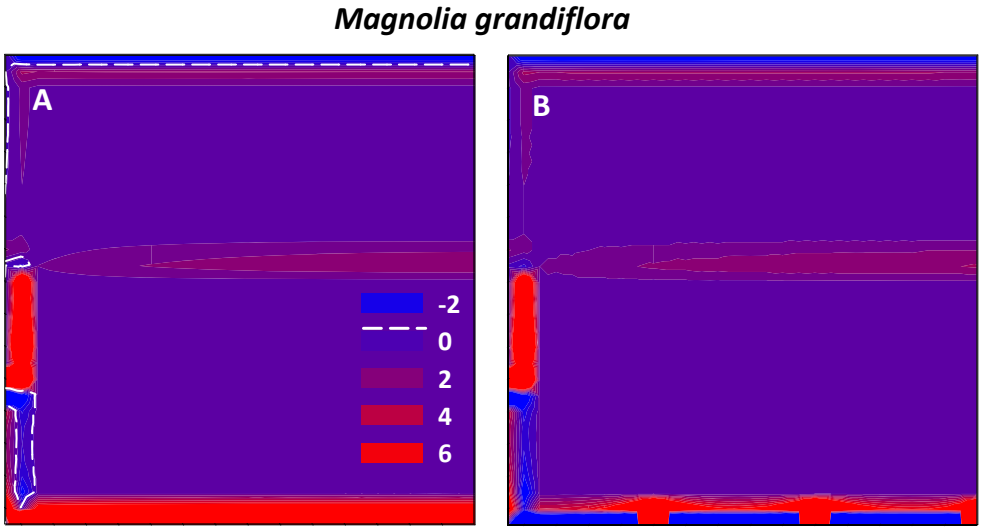

352
353 **Figure S5.** Effect of assuming that transpiration is uniformly distributed among nodes (A) vs.
354 assuming that stomatal transpiration is concentrated in just a few lower-epidermal nodes (B), for
355 *Magnolia grandiflora*. In (B), the stomatal spacing is 69 μm, which is roughly equivalent to a
356 stomatal density of 244 mm^{-2}. Colors represent evaporation rates for each node in the grid,
357 expressed as a percent of the transpiration rate for the leaf area subtended by each node; negative
358 values indicate condensation, and dashed white lines indicate the boundary between regions with
359 net evaporation and regions with net condensation. In A, 22.3% of evaporation occurred from the
360 mesophyll and 67.6% from the lower epidermis; in B, 22.4% occurred from the mesophyll and 65.9%
361 from the lower epidermis (including 94.8% from nodes containing stomata and -28.9%, i.e.,
362 condensation at a rate equal to 28.9% of the total transpiration rate, from nodes between stomata).
363
364

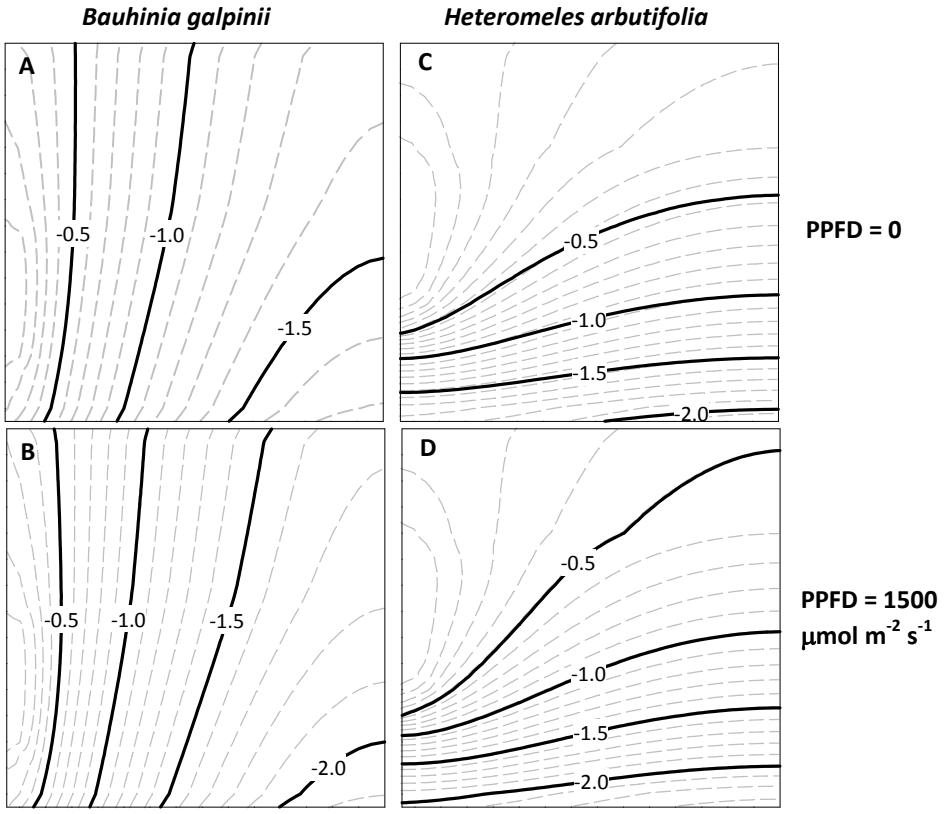

365
366 **Figure S6.** Spatial distributions of water potential in darkness (A, C) and high light (B, D; 1500 μmol
367 m^{-2} s^{-1}) for a thin-leaved species (*B. galpinii*) and a thick-leaved species (*H. arbutifolia*), showing that
368 the influence of leaf thickness on the shape of the predicted water potential profile (being
369 predominantly horizontal in the thin leaf and more vertical in the thick leaf) was similar in darkness
370 and in high light, and was therefore not primarily caused by the occurrence of a larger vertical
371 temperature gradient in the light in the thicker-leaved species.
372
373

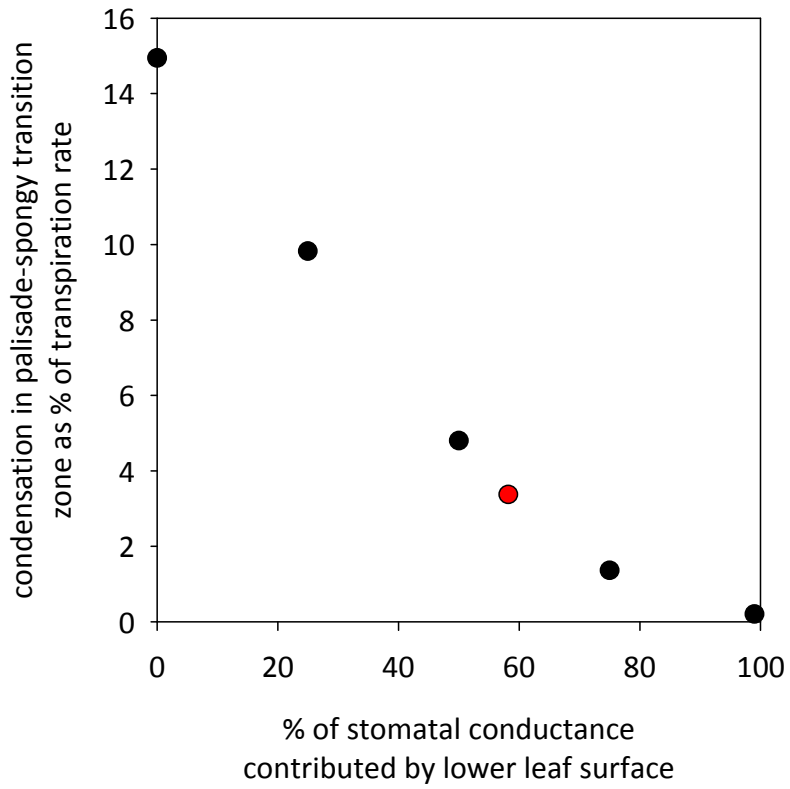

Figure S7. The effect of varying stomatal distribution between the two leaf surfaces on the magnitude of the condensation flux predicted to occur in the leaf center, near the transition between the palisade and spongy mesophyll, in *Helianthus annuus*. The red point represents the observed stomatal distribution for *H. annuus* (58.2% of conductance contributed by the lower surface).

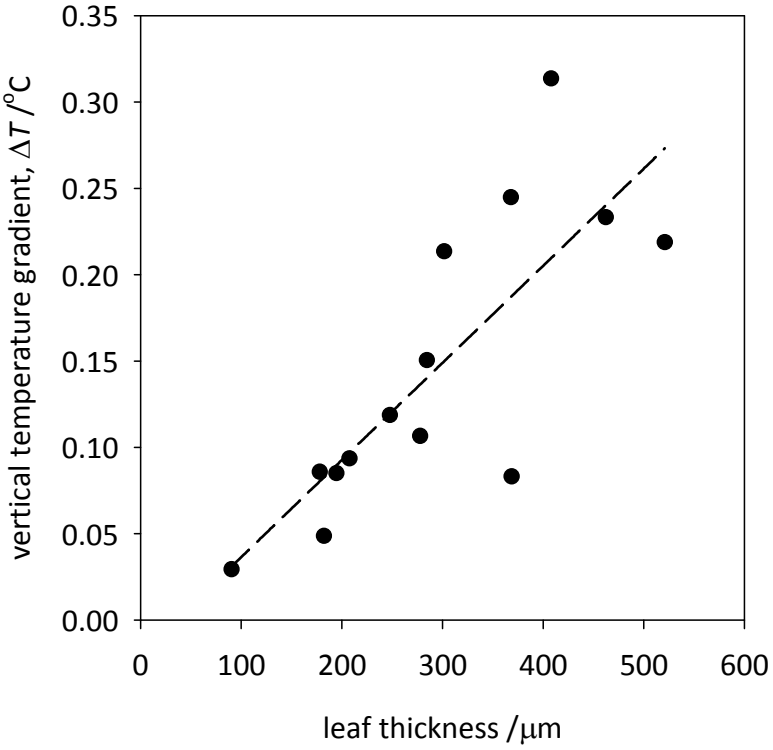

Figure S8. The relationship between leaf thickness and predicted vertical temperature gradient across our 14 study species. The dashed line is a linear regression ((ΔT/°C) = $5.62 \cdot 10^{-4}$·(leaf thickness /μm) – 0.020, r^2 = 0.64, n=14).

IXI. Table S2. List of symbols.

Symbol	Description	Units
a_i	projected area of node i	m^2
b	minus the intercept of linearization of p_{sat} vs T	Pa
AVT	anisothermal vapor transport	-
c_i	intercellular CO_2 concentration	$\mu mol\ mol^{-1}$
$C_{i,top}$	cumulative chlorophyll content at top of node/layer i	$mmol\ m^{-2}$
$C_{i,bottom}$	cumulative chlorophyll content at bottom of node/layer i	$mmol\ m^{-2}$
c_{pair}	heat capacity of air	$J\ mol^{-1}\ K^{-1}$
C_{total}	leaf total chlorophyll content	$mmol\ m^{-2}$
D_{wa}	diffusivity of water vapor in air	$m^2\ s^{-1}$
ΔT	vertical temperature gradient within leaf	^oC
E	leaf transpiration rate	$mmol\ m^{-2}\ s^{-1}$
E_i (**E**)	stomatal transpiration from node i (vector comprising all E_i)	$mol\ s^{-1}$
ε_{leaf}	leaf emissivity to infrared radiation	-
$F_{aniso,ij}$	anisothermal vapor transport from node *i* to node *j*	$mol\ s^{-1}$
F_i (**F**)	net AVT out of node i (vector comprising all F_i)	$mol\ s^{-1}$
F_{ij}	AVT from node i to node j	$mol\ s^{-1}$
f_{TK}	thermal conductivity of cells divided by that of pure water	unitless
g_{bh}	boundary layer conductance to heat	$mol\ m^{-2}\ s^{-1}$
G_i (**G**)	net IVT out of node i (vector comprising all G_i)	$mol\ s^{-1}$
G'_i	G_i plus stomatal transpiration from node i	$mol\ s^{-1}$
g_{bw}	boundary layer conductance to H_2O	$mol\ m^{-2}\ s^{-1}$
g_m	mesophyll conductance to CO_2	$mol\ m^{-2}\ s^{-1}$
g_s	stomatal conductance to H_2O	$mol\ m^{-2}\ s^{-1}$
g_{tw}	total conductance to H_2O	$mol\ m^{-2}\ s^{-1}$
H_i (**H**)	net sensible heat loss from node i (vector comprising all H_i)	$J\ s^{-1}$
H'_i	H_i plus sensible heat loss to air outside of leaf from node i	$J\ s^{-1}$
I_i	shortwave radiation absorbed by node i	$J\ s^{-1}$
I_l	PPFD incident on lower leaf surface	$mmol\ m^{-2}\ s^{-1}$
$I_{NIR,i}$	near infrared radiation absorbed by node i	$J\ s^{-1}$
I_u	PPFD incident on upper leaf surface	$mmol\ m^{-2}\ s^{-1}$
$I_{VIS,i}$	visible radiation absorbed by node i	$J\ s^{-1}$
IVT	isothermal vapor transport	-
k_c	extinction coefficient for PPFD with respect to chlorophyll content	$m^2\ mmol^{-1}$
$K_{f,ij}$ (**K_f**)	conductance for AVT from node i to j (matrix of $K_{f,ij}$)	$mol\ s^{-1}\ K^{-1}$
$k_{g,aniso}$	intrinsic conductivity for AVT	$mol\ s^{-1}\ K^{-1}$
$K_{g,ia}$	conductance for vapor flux from node i to the ambient air	$mol\ s^{-1}\ Pa^{-1}$
$K_{g,ij}$ (**K_g**)	conductance for IVT from node i to j (matrix of $K_{g,ij}$)	$mol\ s^{-1}\ Pa^{-1}$
$k_{g,iso}$	intrinsic conductivity for IVT	$mol\ s^{-1}\ Pa^{-1}$
$K_{h,ia}$	conductance for sensible heat loss from node i to the ambient air	$mol\ s^{-1}\ K^{-1}$
$K_{h,ij}$ (**K_h**)	conductance for sensible heat transfer from node i to j (matrix of $K_{h,ij}$)	$mol\ s^{-1}\ K^{-1}$
K_{leaf}	leaf hydraulic conductance	$mmol\ m^{-2}\ s^{-1}\ Pa^{-1}$
$K_{l,ij}$ (**K_l**)	conductance for liquid water transport from node i to j (matrix of $K_{l,ij}$)	$mol\ s^{-1}\ Pa^{-1}$
K'_1, K'_2	intermediate matrices in solution (Eqns S16a, S17a)	$Pa\ K^{-1}$
K_{ox}	outside-xylem hydraulic conductance	$mmol\ m^{-2}\ s^{-1}\ MPa^{-1}$
K_{plant}	whole-plant hydraulic conductance	$mmol\ m^{-2}\ s^{-1}\ MPa^{-1}$
λ	latent heat of vaporization	$J\ mol^{-1}$
L_i (**L**)	net liquid water loss from node i (vector comprising all L_i)	$mol\ s^{-1}$
p	factor accounting for internal and surface reflectance of PPFD	-
P_m	cell membrane osmotic water permeability	$\mu m\ s^{-1}$
PPFD	photosynthetic photon flux density at adaxial surface	$\mu mol\ m^{-2}\ s^{-1}$
p_{sat}	saturation vapor pressure	Pa
R_a	effective Poiseuille radius of apoplastic nanopathways	nm
R_{gas}	gas constant	$J\ mol^{-1}\ K^{-1}$

Q_i (**Q**)	net radiative energy loss from node i (vector comprising all Q_i)	J s^{-1}
s	slope of linearization of p_{sat} vs T	Pa K^{-1}
σ	Stefan-Boltzmann constant	J K^{-4}
T	temperature	^{o}C or K
τ	leaf transmissivity to PPFD	-
T_{air}	air temperature	^{o}C
t_i	thickness of layer i	m
t	leaf thickness	m
T_i	temperature at node i	^{o}C
T_m	measured leaf temperature (T at lower surface)	^{o}C
T_{sky}	effective sky temperature	K
Vi (**V**)	evaporation from node i	mol s^{-1}
VLA	vein length per unit leaf area	mm^{-1}
V_w	molar volume of water	m^3 mol^{-1}
w_{air}	water vapor mole fraction of ambient air	mol mol^{-1}
w_{avg}	average of w_{air} and w_{leaf}	mol mol^{-1}
w_{leaf}	water vapor mole fraction in leaf intercellular airspaces	mol mol^{-1}
w_{sat}	saturation vapor pressure divided by atmospheric pressure	mol mol^{-1}
w'_s	w_{sat} evaluated at T_m	mol mol^{-1}
ψ	water potential	Pa or MPa
ψ_i (**ψ**)	water potential of node i (vector comprising all ψ_i)	Pa
ψ'_1, ψ'_2	intermediate vectors in solution (Eqns S16b, S17b)	Pa
ψ_{eq}	water potential of an excised, non-transpiring, equilibrated leaf	Pa or MPa

References

Campbell GS, Norman JM (1998) The light environment of plant canopies. *In* An Introduction to Environmental Biophysics. Springer, pp 247-278

Coste S, Baraloto C, Leroy C, Marcon É, Renaud A, Richardson AD, Roggy J-C, Schimann H, Uddling J, Hérault B (2010) Assessing foliar chlorophyll contents with the SPAD-502 chlorophyll meter: a calibration test with thirteen tree species of tropical rainforest in French Guiana. Annals of Forest Science **67:** 607

de Pury DGG, Farquhar GD (1997) Simple scaling of photosynthesis from leaves to canopies without the errors of big-leaf models. Plant, Cell and Environment **20:** 537-557

Evans JR (1998) Photosynthetic characteristics of fast- and slow-growing species. *In* H Lambers, H Poorter, MMI Van Vuuren, eds, Inherent variation in plant growth. Physiological mechanisms and ecological consequences. Backhuys Publishers, Leiden, The Netherlands, pp 101-119

Feret J-B, François C, Asner GP, Gitelson AA, Martin RE, Bidel LP, Ustin SL, le Maire G, Jacquemoud S (2008) PROSPECT-4 and 5: Advances in the leaf optical properties model separating photosynthetic pigments. Remote Sensing of Environment **112:** 3030-3043

Gates DM, Keegan HJ, Schleter JC, Weidner VR (1965) Spectral properties of plants. Applied optics **4:** 11-20

Jacob J, Lawlor D (1991) Stomatal and mesophyll limitations of photosynthesis in phosphate deficient sunflower, maize and wheat plants. Journal of Experimental Botany **42:** 1003-1011

Jacquemoud S, Baret F (1990) PROSPECT: A model of leaf optical properties spectra. Remote sensing of environment **34:** 75-91

Markwell J, Osterman JC, Mitchell JL (1995) Calibration of the Minolta SPAD-502 leaf chlorophyll meter. Photosynthesis research **46:** 467-472

Scoffoni C, Albuquerque C, Brodersen CR, Townes SV, John GP, Bartlett M, Buckley TN, McElrone AJ, Sack L (in press) Outside-xylem vulnerability, not xylem embolism, controls leaf hydraulic decline during dehydration. Plant Physiology **in press**

Scoffoni C, Vuong C, Diep S, Cochard H, Sack L (2014) Leaf shrinkage with dehydration: coordination with hydraulic vulnerability and drought tolerance. Plant physiology **164:** 1772-1788

Ustin SL, Jacquemoud S, Govaerts Y (2001) Simulation of photon transport in a three-dimensional leaf: implications for photosynthesis. Plant, Cell and Environment **24:** 1095-1103